Sliding mode based adaptive linear neuron proportional resonant control of Vienna rectifier for performance improvement of electric vehicle charging system

Ahmed, Hafiz; Çelik, Doan

Journal of Power Sources

Peer reviewed version

Cyswllt i'r cyhoeddiad / Link to publication

23. Jul. 2023

Sliding Mode Based Adaptive Linear Neuron Proportional Resonant Control of Vienna Rectifier for Performance Improvement of Electric Vehicle Charging System

Hafiz Ahmed[a,*], Doğan Çelık[b,*]

[a]*Nuclear Futures Institute, Bangor University, Bangor LL57 2DG, UK*
[b]*Department of Electrical and Electronics Engineering, Van Yuzuncu Yıl University, Van 65080, Turkey*

Abstract

With a strong expansion of transportation electrification, electric vehicle charging systems are becoming very important part of the electrified powertrain. This paper proposes a sliding mode based adaptive linear neuron (ADALINE)-proportional resonant (PR) control solution to enhance performance of Vienna rectifier (VR), an AC-DC converter, as a charger for series-linked battery packs of electric vehicles (EVs) operating under unbalanced and distorted grid conditions. A sliding-mode control (SMC) has been utilized for the fast and robust regulation of DC-link voltage while ADALINE-PR control is proposed to regulate the source current errors through the real-time adaptation of the controller gains. Another contribution of this paper is to derive reference current signals without complex positive and negative sequences component separation, coordinate transformation and phase-locked loop. Besides, constant and pure battery current during charging/discharging is achieved in contrast to the previous studies. The proposed control algorithm achieves superior dynamic and steady-state performances and eliminate harmonics of source currents and ripples in active power, DC-link voltage and battery current compared to the existing studies. The proposed method has been implemented in a digital signal processor (DSP) TMS320F28335 within a processor in the loop (PIL) quasi-real-time setting. Extensive comparative results demonstrate the effectiveness of proposed control algorithm.

Keywords: Vienna Rectifier, EV Charging, Sliding Mode Control, Proportional Resonant Control, ADALINE, Harmonics

1. Introduction

Renewable energy sources can contribute significantly towards decarbonization of the energy production. This has motivated many researchers to focus on improving the performance of renewable energy systems such as solar, wind, geothermal etc. For recent developments in performance improvement of solar cells, interested readers may consult [1–5]. In addition to energy production decarbonization, energy consumption also needs to be decarbonized [6–8]. Transportation sector produces a significant portion of the global carbon emission. Electric vehicles (EVs) are going to play a key role in transport decarbonization, which is essential to ensure net-zero carbon emission by 2050. Large-scale adoption of EVs will require significant investment in the charging infrastructure development. However, the existing distribution networks are not developed by taking into account the large-scale deployment of charging infrastructures. As such, integrating charging stations into distribution networks can result in voltage profile degradation, harmonic distortions,

and an increase in peak load [9–12]. In addition, power flow between energy storage and the grid through vehicle-to-home/-building (V2H/B), bidirectional vehicle-to-grid (V2G) and unidirectional controlled charging (V1G) etc. can lead to current distortions in the utility grid. Effective integration of EVs into the power network can be carried out through appropriately controlled grid-interfaced power electronic converter-based charging stations or charger, which performs a central role in the V2G, grid-to-vehicles (G2V) operations, and integration of the renewable energy into the smart-grid. In this context, any control strategy for EV charger should have the capability to substantially reduce the ripples in the DC-voltage and current, keep the harmonic distortion at an acceptable level and improve the power quality at the AC and DC sides.

AC-DC converters play an important role in converting the AC grid voltages into DC voltage, which will ultimately be responsible for charging the battery packs. Owing to its importance in EV charging, numerous converter topologies are reported in the literature. Some of the popular converter topologies are bidirectional AC/DC converters, transformer rectifier units, passive rectifiers, power factor correction with boost rectifiers and rectifiers. However, these rectifier topologies are often incapable to provide DC power at a high power factor (PF) together low harmonic distortion. In addition, these topologies of-

---

*The authors have contributed equally and the authorship is in alphabetical order

**Corresponding author

Email address: dogancelik@yyu.edu.tr (Doğan Çelık)

Nomenclature

ΔI_i	Percent ripple of AC current	ADALINE	Adaptive linear neuron
$\Delta \tilde{v}_{o,dc}$	Percent ripple of the DC-link voltage	AFE	Active front-end
η	Converter efficiency	BEV	Battery electric vehicle
μ_i	Learning rate	CCS	Code composed studio
ζ	Sliding surface	DF	Displacement power factor
$C_{1,2}$	DC-link capacitors	DF	Distortion factor
d_{conv}	Duty cycle of the DC-DC converter	DSP	Digital signal processor
f	Grid frequency	EPLL	Enhanced Phase-Locked Loop
f_{sw}	Switching frequency	EV	Electric vehicle
i_n	Negative DC-link current	GA	Genetic algorithm
i_o	Mid-point current	LG	Line to line ground
i_p	Positive DC-link current	LLG	Line to ground
$I_{bat}^\star$	Reference battery current	NN	Neural network
L_f	Line inductance	PF	Power factor
$P^\star$	Active power reference	PI	Proportional integral
$Q^\star$	Reactive power reference	PIL	Processor in the loop
R_f	Series resistance at the AC-side	PLL	Phase-locked loop
S	Apparent power	PR	Proportional resonant
$S_{ip}, S_{i}o$ and $S_{i}n$	Positive, neutral and negative poles	PSO	Particle swarm optimization
u_{abc} and i_{abc}	Grid voltages and currents	SMC	Sliding-mode control
u_g	Grid line to line RMS voltage	THD	Total harmonic distortion
v_{mo}	Mid-point voltage	V1G	Unidirectional controlled charging
$v_{o,dc}$	DC-link voltage	V2G	Vehicle-to-grid
W_1 and W_2	ADALINE weight vectors	V2H/B	Vehicle-to-home/-building
x	a, b, c phases	VR	Vienna rectifier
$i_{D(A,B,C)+}$ and $i_{D(A,B,C)-}$	Currents flowing through the upper and lower diodes, respectively.		

ten have large size and can be quite heavy. Out of the various topologies reported in the literature, the three-phase three-level Vienna rectifier (VR) has become very popular in recent times. Even numerous commercial power semiconductor manufacturers also provide reference designs for this topology, which indicates the popularity of this topology for industrial applications as well. This topology is relatively simple and requires six switches (IGBT or MOSFET) and six diodes. Thanks to the three-level operation, the voltage stress across each diode and switch are $v_{dc}/2$, where v_{dc} is the DC-link voltage. The VR is fed by the AC grid. As such, grid voltage issues like unbalanced and distorted grid greatly affect the performance of this rectifier. To mitigate the effect of grid voltage and load-side disturbances, an effective control strategy is needed that can not only improve the power quality but also has a fast

and robust response to any change and/or disturbances.

Authors in [13] proposed the application of disturbance observer and PLL for high-perfrmance control of EV charging station. PLL-based solutions can often under perform in a weak grid due to PLL limitations. Moreover, as highlighted in [14], conventional disturbance observer can be sensitive to measurement noise. In [15], an extended state observer is used for the estimation of load currents for control of the VR. In [16], a second-order generalized integrator frequency-locked loop based controller is proposed for the VR. This controller can handle unbalanced and distorted grid voltage; however, the overall control structure is linear and non-adaptive. As such, there is scope to improve the robustness and response time. In [17], a synchronous reference frame current controller is proposed for the VR. However, this controller does not take into account

the effects caused by an unbalanced grid. Similar approach has been considered in [18]. The presence of PLL makes this controller sensitive to weak grid. Moreover, no validation results are presented for unbalanced grid. It is well known that unbalanced grid voltage causes ripple in the DC-Link capacitor, resulting in energy loss and reduction of capacitor lifetime. Detailed stability analysis of synchronous reference frame control method for the VR has been conducted in [19]. A voltage sensor-less control scheme for the active rectifier has been proposed in [20]. In this method, accurate value of the per-phase inductor is required. Aging of inductor causes it's value to change. As such, inaccurate sensing is inevitable in the long run, thereby causing large steady-state error. A generalized Clarke transformation-based synchronous reference frame control method is proposed in [21]. In this approach, three orthogonal signal generator PLLs are used. This can be computationally expensive for real-time implementation.

In [22], a modified proportional resonant controller is proposed to reduce the current total harmonic distortion (THD). The controller proposed in [22] is applied in the natural frame. So, one controller for each phase is required. In addition, five parallel compensators are applied per-phase to effectively eliminate the harmonics up to 13th-order. As such, the overall control solution is very computationally complex. In [23], a phase-locked loop (PLL) based model predictive control method has been applied to the VR. Despite possessing some excellent characteristics, this controller is not designed for an unbalanced grid operation. An extension of this work has been presented in [24] for unbalanced DC-link voltage. Although this improves the neutral-point voltage ripple, however, uncertainty in the system parameter value increases the overall total harmonic distortion, which not preferable.

An active disturbance rejection DC-link voltage controller together with a model predictive current controller is proposed in [25]. Model predictive controller requires an accurate model of the plant. System parameters typically change due to aging. As such, this controller may face difficulty in the long run if there is a significant parameter mismatch. A computationally efficient model predictive controller is proposed in [26] which depends on the PLL. In a weak grid, PLL-based operation can be problematic. In [27], a deadbeat predictive controller is proposed for the current control of the VR; however, this controller requires an accurate value of the system inductor. Large parameter variation may introduce significant steady-state error. An enhanced PLL (EPLL)-based control strategy for the VR is proposed in [28]. Due to the lack of gain-normalization term in EPLL, it has a slow convergence when there is a voltage sag. This can make the system slowly responsive in the presence of sudden voltage sag. In [29], a rule-based current control method is proposed for PWM controlled rectifiers. The lack of an actual feedback regulator may make the system vulnerable to parameter variations and/or disturbances.

A three-layer model-predictive based controller is pro-posed in [30] to reduce the current ripple and distortion and to provide neutral voltage balance. However, this controller is computationally complex and requires a lot of information and mathematical computations. Besides, conventional reference current calculation method has been used for AC current control, which does not achieve good performance under grid disturbances. Computational complexity can be limiting factor for the low-cost system based embedded implementation. An online identification-based control strategy for PWM controlled rectifiers is proposed in [31]. However, this approach requires the implementation of filtering methods such as cascaded delayed signal cancellation and second-order generalized integrator. Real-time implementation of these filters can be complicated as numerous filters are used. In [32], an improved sliding mode control technique with artificial neural network-based uncertainty estimation has been proposed for the VR. This controller requires numerous parameter to tune. Moreover, very limited validation results are presented. A similar discontinuous control approach has been presented in [33]. An improved PWM method for the VR with LCL-filter has been proposed in [34].

A key issue that makes the operation of VR in unbalanced grid challenging is the appearance of double the fundamental frequency ripples or oscillations in the DC-link. These ripples or oscillations propagate to the rest of the system and deteriorate the power quality and also reduce the lifetime of the capacitor. Moreover, to address the ripples, a large value capacitor is also required which increases the cost and loss, thereby reducing the efficiency. In [13], the reference calculation is based on using PLL. As such, filtering is unavoidable. Moreover, complex algebra is also used to calculate the reference. The study reported in [16] proposed the application of the adaptive filtering-based grid-synchronization method for unbalanced grid induced oscillation-free reference current generation. A similar approach has been considered in [28], however, here enhanced PLL is used as the grid-synchronization method. In [29], a quarter-delayed based compensation power reference generation method is considered by employing complex signal transformation. In [35], a proportional-resonant controller is used with two times the grid frequency being considered as the resonant frequency. This controller is used in the DC-link to mitigate the negative effect of voltage ripple.

In this paper, a comprehensive control solution is proposed for the VR converter operating in an unbalanced and distorted grid to improve the performance of the VR converter for the EV charging stations. To mitigate the effect of an unbalanced and distorted grid, a simple reference current calculation based on the sliding-mode control (SMC) and adaptive linear neuron (ADALINE) proportional resonant (PR) control is proposed that doesn't require any complex filtering, mathematical transformation and PLL. To generate the active power reference, a SMC strategy is applied for the DC-link voltage regulation. Finally, the ADALINE PR control is applied for the current regulation and to generate the switching pulses for
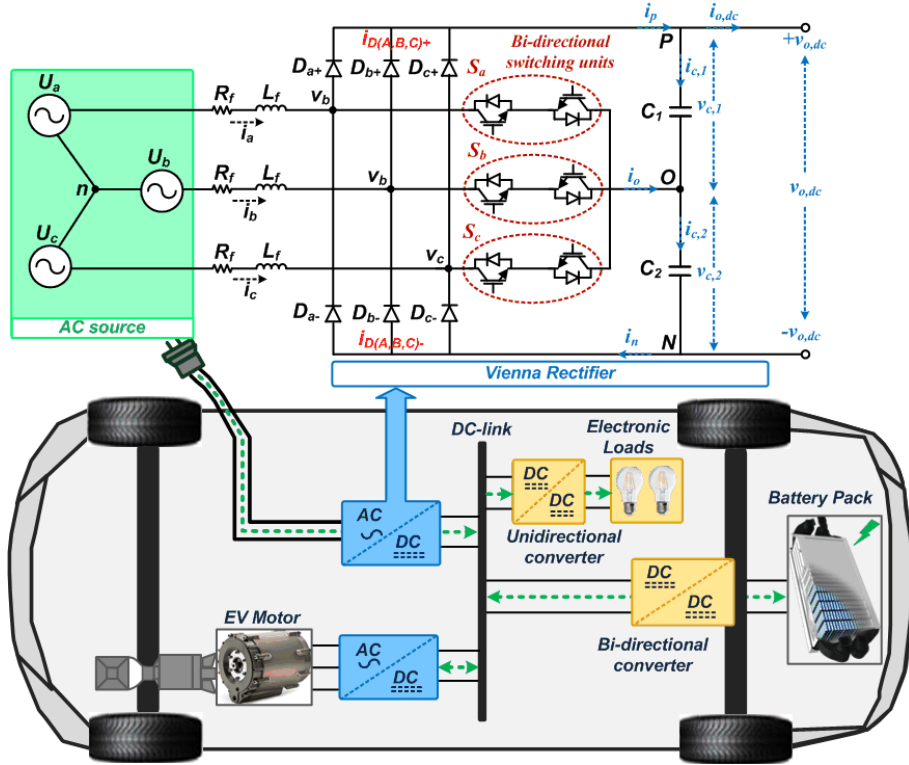
Figure 1: Topology of the considered EV charging system.

the VR converter. Unlike conventional PR, the proposed ADALINE PR control uses a real-time adaptation of the proportional and resonant gains through the ADALINE method. Integration of the ADALINE with PR makes the overall current controller very fast responsive. Besides, the active power, DC-link voltage, battery charging current, the DC-line current and load current are protected from second order harmonic ripples against various grid disturbances. In addition to these, the proposed control algorithm is able to successfully compensate the imbalanced and distorted currents caused by the non-linear load. The detailed mathematical analyses for the derivation of second-order harmonic voltage expressions in the DC-link and online tuning of the proportional and resonant gains with the ADALINE are provided.

In summary, compared to the previous studies, the proposed control algorithm achieves quite superior characteristics and performance in terms of, fast dynamic response, lower ripples in the active power, the DC-link voltage and battery current, reducing algorithm complexity, and lower THD of the line currents as well as providing near unity PF and lower computational burden. A new current regulation control, called ADALINE PR control has been proposed to regulate AC line currents instead of the conventional PR, PI control and any other standard controllers while the SMC has been employed for the DC-link voltage regulation. Another contribution of this paper is to generate reference line current to overcome disturbances at the AC-side and DC-side without sequence

extraction. Comprehensive evaluation tests such as unbalanced and distorted grid conditions, unbalanced DC-link, and a stepped change in the DC-link voltage and DC load have been performed based on the DSP based PSIM-PIL semi-experiment set up to verify the effectiveness and feasibility of the proposed control algorithm.

The rest of this article is organized as follows: Sec. 2 gives an overview of the considered EV charging system, Sec. 3 presents in detail the proposed control method, results are discussed in Sec. 4, and finally, Sec. 5 concludes this paper.

2. The structure of the EV Charging System

In this paper, a three-phase VR converter is adopted in the EVs charging system as depicted in Fig. 1, to fulfill slow and fast charging demands in various electric grid conditions [36]. The topology of the VR consists of six diodes and three bidirectional switching units (S_a, S_b and S_c). The AC side of the VR is tied to the AC grid, and the DC side is tied to the battery electric vehicle (BEV) and electronic load. In Fig. 1, u_{abc} and i_{abc} are grid phase voltages and currents, $+v_{dc}$ and $-v_{dc}$ represent the upper and lower DC-link capacitor voltages and R_f and L_f denote equivalent series resistance and the filter inductance, respectively. The three bidirectional switching units can represent the VR states as:

$$S_x = \begin{cases} 0 & S_x \text{ ON}, S_{xp} = 0, S_{x0} = 1, S_{xn} = 0 \\ 1 & S_x \text{ ON } i_x > 0, S_{xp} = 1, S_{x0} = 1, S_{xn} = 0 \\ -1 & S_x \text{ OFF} i_x > 0, S_{xp} = 0, S_{x0} = 0, S_{xn} = 1 \end{cases} \tag{1}$$

where $x = a, b, c$ are the individual phases. The switch function S_x is divided into three single-pole as S_{ip}, S_{io} and S_{in}. The DC-link voltage of the VR, $v_{o,dc}$ is separated by two voltages as $v_{c,1}$ and $v_{c,2}$ as described in Fig. 1. The control algorithms should provide the balance DC-link voltage to decrease the voltage stress across the switches [25, 28, 30]. The dynamic states of the AC-side and DC-side can be written depending on the operation principle of the VR as:

$$\begin{cases} u_x = R_f i_x + L_f \frac{di_x}{dt} + v_{xo} + v_{ON} \\ C_1 \frac{dv_{c,1}}{dt} = S_{ap} i_a + S_{bp} i_b + S_{cp} i_c - i_{o,dc} \\ C_2 \frac{dv_{c,2}}{dt} = -S_{an} i_a - S_{bn} i_b - S_{cn} i_c - i_{o,dc} \end{cases} \tag{2}$$

where $i_{o,dc}$ denotes the DC-link current. The output x-phase voltage (referred to as mid-point o) v_{xo} can be expressed based on the switching states and AC supply current as follows:

$$v_{xo} = (1 - S_x) \left(\frac{\text{sign}(i_x) + 1}{2} v_{c,1} + \frac{\text{sign}(i_x) - 1}{2} v_{c,2} \right) \tag{3}$$

The relationship between DC side mid-point and AC side voltage neutral point voltage is represented by eq. (4) [26]:

$$v_{ON} = -\frac{1}{3} \left(\sum_{x=a,b,c} S_{xp} v_{c,1} - \sum_{x=a,b,c} S_{xn} v_{c,2} \right) \tag{4}$$

The relationship between the neutral point of AC supply and the voltage at the rectifier diode clamp point can be expressed by eq. (5) according to the circuit knowledge [25]:

$$v_{xN} = v_{xo} + v_{ON},$$
$$= \left(S_x - \frac{1}{3} \sum_{x=a,b,c} S_{xp} \right) v_{c,1} +$$
$$\left(-S_{xn} + \frac{1}{3} \sum_{x=a,b,c} S_{xn} \right) v_{c,2} \tag{5}$$

From eq. (1), the state-space equations for the AC and DC sides of the VR are given in the stationary reference frame $(\alpha - \beta)$ for analysis of the resonant control as:

$$\begin{cases} e_{\alpha\beta} = R_f i_{\alpha\beta} + L_f \frac{di_{\alpha\beta}}{dt} + v_{\alpha\beta} \\ C_1 \frac{dv_{c,1}}{dt} = S_{\alpha p} i_\alpha + S_{\beta p} i_\beta - i_{o,dc} \\ C_2 \frac{dv_{c,2}}{dt} = -S_{\alpha n} i_\alpha - S_{\beta n} i_\beta - i_{o,dc} \end{cases} \tag{6}$$

Based on the Kirchhoff's current law, the currents flowing the positive DC-link (i_p) and the negative DC-link (i_n) are defined by eq. (7) [22]:

$$i_p = i_{DA+} + i_{DB+} + i_{DC+}$$
$$i_n = i_{DA-} + i_{DB-} + i_{DC-} \tag{7}$$

where $i_{D(A,B,C)+}$ and $i_{D(A,B,C)-}$ represent the currents flowing through the upper and lower diodes, respectively. The currents via the top and bottom diodes of positive and negative current polarities are expressed depending on the switching states and source currents as [22]:

$$i_{D(A,B,C)+} = (1 - S_x) i_x, i_x > 0$$
$$i_{D(A,B,C)-} = -(1 - S_x) i_x, i_x < 0 \tag{8}$$

According to the switching states and source currents, the DC-link currents and mid-point current are expressed by eq. (9) and eq. (10) as:

$$i_p + i_n = \sum_{x=a,b,c} (1 - S_x) \text{sign}(i_x) i_x \tag{9}$$

$$i_o = \sum_{x=a,b,c} S_x i_x \tag{10}$$

where i_o is mid-point current. Considering balanced DC-link voltage, the DC-link capacitances, C_1 and C_2 are supposed to be equal, i.e., $C_1 = C_2 = C$. The mid-point voltage v_{mo} of the VR can be given based on the upper and lower DC capacitor voltages [23]. The dynamic equation of the mid-point voltage is given as follows:

$$C \frac{dv_{mo}}{dt} = C \frac{d(v_{c,1} - v_{c,2})}{dt} = -i_o \tag{11}$$

3. The Proposed Control Scheme

In this section, the proposed control algorithm is separated into four major blocks for the VR: i) sliding mode control for the DC-link voltage regulation, ii) ADALINE PR current control loop, iii) battery current control, and iv) reference current generation for compensation of the active power ripple and the DC-link voltage and current ripples.

3.1. Sliding mode control for DC-link voltage regulation

The DC-link voltage control performs an important role in ensuring the fast dynamic performance of the VR. A fast responsive and robust control method for the DC-link voltage can make the response of the system less sensitive to changes in system parameters and load-side and/or source-side (i.e. grid voltage) change [37]. In this study, a SMC method is applied for the fast and robust regulation of the DC-link voltage of the VR. This controller acts as the outer-loop controller and its focus is to reduce the

voltage ripple in the DC-link capacitor, which contributes to reducing the size and cost of the capacitor. Moreover, a reduction in capacitor size also contributes to lowering the loss, thereby increasing the overall efficiency of the system. As the DC-link controller is used in the outer loop, it's job is to generate the reference power which will then be used by the current controller for the generation of switching pulses.

The relationship between AC side active power and DC side power can be obtained with multiply both sides of eq. (6) as follows:

$$v_{o,dc} \frac{(S_{\alpha p} - S_{\alpha n}) i_\alpha + (S_{\beta p} - S_{\beta n}) i_\beta}{2} =$$
$$\frac{C}{2} \frac{v_{o,dc} dv_{o,dc}}{dt} + v_{o,dc} i_{o,dc} \qquad (12)$$

While the right side of eq. (12) represents the sum of the capacitor and the load powers, the left side of eq. (12) is the link between the AC and the DC sides. Neglecting power loss, the active power consumed on the DC side $(P_{o,dc})$ is equivalent to the active power supplied on the AC side $(P_{i,ac})$.

$$P_{i,ac} = P_{o,dc} = \frac{C}{2} \frac{v_{o,dc} dv_{o,dc}}{dt} + v_{o,dc} i_{o,dc} \qquad (13)$$

After rearranging the expression of eq. (13), the output power $P_{o,dc}$ can be given by eq. (14) [16, 31]:

$$p_{i,ac} = p_{o,dc} = \frac{1}{4} \frac{dv_{o,dc}^2}{dt} + \frac{v_{o,dc}^2}{R} \qquad (14)$$

where R denotes load at the DC-side. The active power including power ripples at the DC-side can be expressed by eq. (15). A detailed analysis of the power ripples is given in Section 3.2.

$$P_{o,dc} = p_{o,dc} + p_{c2} \cos(2\omega t) + p_{s2} \sin(2\omega t)$$
$$= p_{o,dc} + p_{2\omega} \cos(2\omega t - \varphi) \qquad (15)$$

where

$$P_{2\omega} = \sqrt{p_{c2}^2 + p_{s2}^2}, \varphi = \tan^{-1}(p_{s2}/p_{c2}) \qquad (16)$$

The DC-link voltage can be computed by inserting eq. (15) and eq. (16) into eq. (14) as follows:

$$v_{o,dc}^2(t) = \underbrace{K \exp\left(\frac{-4t}{RC}\right)}_{\text{Transient}} \underbrace{R p_{o,dc}}_{\text{Constant}}$$
$$\underbrace{\frac{2R P_{2\omega}}{\sqrt{(\omega RC)^2 + 4}} \cos\left\{2\omega t - \varphi - \tan^{-1}\left(\frac{\omega RC}{2}\right)\right\}}_{\text{2}^{\text{nd}}\text{ harmonic }(2\omega)}$$
$$(17)$$

The expression of eq. (17) comprises of a constant DC term, a transient term and second-order harmonic term. By ignoring the transient response and taking into consideration only the steady-state, it is obvious that the active power ripples are reflected as ripples in the DC-link voltage.

The SMC takes the DC side voltage of the VR as the active power reference value $P^\star$, while the reactive power reference value has been taken as a constant 0. To develop the sliding-mode voltage controller, the DC-link voltage regulation error $\Delta \tilde{v}_{o,dc}$ is considered as a state variable and given by eq. (18):

$$\zeta_1 = \Delta \tilde{v}_{o,dc} = v_{o,dc}^\star - v_{o,dc} \qquad (18)$$

where $v_{o,dc}^\star$ is the reference DC-link voltage. Derivative of the first state variable, which is also the second state variable is $\zeta_2 = \dot{\zeta}_1$. For the DC-link dynamics, the following proportional-derivative-type sliding-surface is considered:

$$\sigma(\zeta) = \eta_1 \zeta_1 + \eta_2 \zeta_2 \qquad (19)$$

where $\zeta = \begin{bmatrix} \zeta_1 & \zeta_2 \end{bmatrix}^T$ and the sliding surface tuning parameters are given by η_1 and η_2 which are both positive constants. Then, depending on the polarity of the sliding surface and state variables, the switching states are calculated as [38]:

$$\xi_1 = \begin{cases} 1, & \sigma(\zeta) \zeta_1 > 0 \\ -1, & \sigma(\zeta) \zeta_1 < 0 \end{cases} \qquad (20)$$

$$\xi_2 = \begin{cases} 1, & \sigma(\zeta) \zeta_2 > 0 \\ -1, & \sigma(\zeta) \zeta_2 < 0 \end{cases} \qquad (21)$$

Using the switching states and the state variables, the output of the DC-link voltage controller can be calculated as:

$$\xi = \zeta_1 \xi_1 + \zeta_2 \xi_2 \qquad (22)$$

The output of the sliding-mode controller can then be used to generate the reference active power as:

$$P^\star = \xi^2 sign(\zeta) \qquad (23)$$

where signum is the conventional signum function, i.e., $sign(\xi) = \xi/|\xi|$. Thanks to the considered proportional-derivative-type sliding surface, the considered SMC can be robust to disturbances. Moreover, the use of signum function makes it suitable to eliminate the steady-state error. To make the reference power smooth, a low cut-off frequency low-pass filter is added as a trade-off between fast dynamic response versus smooth response.

3.2. Reference current derivation for compensation of ripples

One of the key aspect of the proposed control method is to derive current references to ensure enhance dynamic performance under unbalanced and harmonically distorted

grid. In this paper, instead of separating complex positive and negative sequences, coordinate transformations and using PLL, the power compensation values are derived by the grid voltage and current signals and their quadrature signals obtained through quarter-delays.

Assuming that y is a variable in the stationary reference frame, its quadrature signals with 90° phase shift can be given as follows [29, 39]:

$$y_\perp = y_{\alpha\beta\perp}^+ + y_{\alpha\beta\perp}^- = -jy_{\alpha\beta}^+ + jy_{\alpha\beta}^- \qquad (24)$$

The relationship between positive and negative sequences and quadrature signals are given as follows:

$$\begin{bmatrix} y \\ y_\perp \end{bmatrix} = \begin{bmatrix} 1 & 1 \\ -j & j \end{bmatrix} \begin{bmatrix} y_{\alpha\beta}^+ \\ y_{\alpha\beta}^- \end{bmatrix} \qquad (25)$$

The inverse of eq. (25) is expressed by eq. (26):

$$\begin{bmatrix} y_{\alpha\beta}^+ \\ y_{\alpha\beta}^- \end{bmatrix} = \frac{1}{2} \begin{bmatrix} 1 & j \\ 1 & -j \end{bmatrix} \begin{bmatrix} y \\ y_\perp \end{bmatrix} \qquad (26)$$

Active and reactive powers with their ripples depending on the quadrature signals are written by the grid voltage and current in the following [39]:

$$\begin{cases} p = \frac{1}{2}\left(i_\alpha u_\alpha + i_\beta u_\beta + i_{\alpha\perp} u_{\alpha\perp} + i_{\beta\perp} u_{\beta\perp}\right) \\ p_{c2} = \frac{1}{2}\left[m_1 \cos\left(2\omega t\right) + m_2 \sin\left(2\omega t\right)\right] \\ p_{s2} = \frac{1}{2}\left[m_1 \sin\left(2\omega t\right) - m_2 \cos\left(2\omega t\right)\right] \\ q = \frac{1}{2}\left(i_\alpha u_\beta - i_\beta u_\alpha + i_{\alpha\perp} u_{\beta\perp} - i_{\beta\perp} u_{\alpha\perp}\right) \\ p_{c2} = \frac{1}{2}\left[m_3 \cos\left(2\omega t\right) + m_4 \sin\left(2\omega t\right)\right] \\ p_{s2} = \frac{1}{2}\left[m_3 \sin\left(2\omega t\right) - m_4 \cos\left(2\omega t\right)\right] \end{cases} \qquad (27)$$

where

$$\begin{cases} m_1 = i_\alpha u_\alpha + i_\beta u_\beta - i_{\alpha\perp} u_{\alpha\perp} - i_{\beta\perp} u_{\beta\perp} \\ m_2 = i_\alpha u_{\alpha\perp} + i_\beta u_{\beta\perp} + i_{\alpha\perp} u_\alpha + i_{\beta\perp} u_\beta \\ m_3 = i_\alpha u_\alpha - i_\beta u_\beta - i_{\alpha\perp} u_{\alpha\perp} + i_{\beta\perp} u_{\beta\perp} \\ m_4 = i_\alpha u_{\beta\perp} - i_\beta u_{\alpha\perp} + i_{\alpha\perp} u_\beta - i_{\beta\perp} u_\alpha \end{cases} \qquad (28)$$

Since the ripples in the DC-link voltage are concerned with the ripples in the active power on the converter side, the aim of the control algorithm can be theoretically demonstrated. The derivation of the current reference for compensation ripples in the active power can be expressed as follows [27]:

$$\begin{pmatrix} i_\alpha^* \\ i_\beta^* \\ i_{\alpha\perp}^* \\ i_{\beta\perp}^* \end{pmatrix} = \frac{P^\star}{\partial_p} \begin{pmatrix} u_{\beta\perp} \\ -u_{\alpha\perp} \\ -u_\beta \\ u_\alpha \end{pmatrix} \qquad (29)$$

where $\partial_p = u_\alpha u_{\beta\perp} - u_\beta u_{\alpha\perp}$ and $\partial_p \neq 0$ [27]. To mitigate active power ripples, the control target should be provided by (30):

$$\begin{cases} p_{\text{comp}} = 0 \quad m_1 = m_2 = 0 \\ q_{\text{comp}} = P^* \frac{u_\alpha u_{\alpha\perp} + u_\beta u_{\beta\perp}}{\partial_p} \end{cases} \qquad (30)$$

As given by eq. (31), another control target is to derive current reference for mitigating ripples in the reactive power to ensure stable operation:

$$\begin{pmatrix} i_\alpha^* \\ i_\beta^* \\ i_{\alpha\perp}^* \\ i_{\beta\perp}^* \end{pmatrix} = \frac{2P^\star}{\partial_q} \begin{pmatrix} u_\alpha \\ u_\beta \\ u_{\alpha\perp} \\ u_{\beta\perp} \end{pmatrix} \qquad (31)$$

where $\partial_q = u_\alpha^2 + u_\beta^2 + u_{\alpha\perp}^2 + u_{\beta\perp}^2$ and $\partial_q \neq 0$. Similarly, the control target can be achieved by eq. (32) to reduce reactive power ripples:

$$\begin{cases} p_{\text{comp}} = P^* \frac{u_\alpha^2 + u_\beta^2 - u_{\alpha\perp}^2 - u_{\beta\perp}^2}{\partial_q} \\ q_{\text{comp}} = 0 \quad m_3 = m_4 = 0 \end{cases} \qquad (32)$$

In literature, conventional reference current has commonly been employed to control the input current of the converter. However, it does not operate under unbalanced DC-link, grid disturbances such as unbalanced and distorted grid voltages, properly. The reference input currents are computed by Eq. (33) as follows [30]:

$$\begin{pmatrix} i_a^\star \\ i_b^\star \\ i_c^\star \end{pmatrix} = \frac{1}{\partial_c} \begin{pmatrix} u_\alpha & u_\beta \\ u_\beta & -u_\alpha \end{pmatrix} \begin{pmatrix} P^\star \\ Q^\star \end{pmatrix} (\alpha\beta/abc) \qquad (33)$$

where $\partial_c = u_\alpha^2 + u_\beta^2$.

3.3. ADALINE PR control for AC current regulation

In this study, stationary reference frame current control method, i.e., controlling the currents directly in the $\alpha\beta$-frame is considered. Since the reference currents are sinusoidal in the stationary reference frame, proportional-resonant (PR) is often considered a suitable choice to ensure zero steady-state error instead of the conventional proportional integral (PI) controller [40, 41]. The transfer function of a continuous-time PR controller with damping is given by [42]:

$$\begin{aligned} G_{PR}(s) &= G_{PR}(s) \\ &= \kappa_p + \kappa_r \underbrace{\frac{2\Omega_c s}{s^2 + 2\Omega_c s + \Omega^2}}_{G_r(s)} \end{aligned} \qquad (34)$$

where κ_p and κ_r are the proportional and resonant gains, Ω_c is the cut-off frequency and Ω is the resonant frequency. Transfer function given by eq. (34) is in the continuous-time and not suitable for real-time implementation in embedded devices. So, discretization of the transfer function is necessary. In the literature, the Tustin method is often recommended where the continuous-time operator s can be replaced by it's digital equivalent as $s = T_s(z-1)/(z+1)$ with T_s being the sampling frequency and the forward shift operator is denoted by z. In the

discrete-time, the transfer function of the PR controller with damping is given by:

$$G_{PR}(z) = \frac{n_1\left(1 - z^{-2}\right)}{d_0 + d_1 z^{-1} + d_2 z^{-2}} \qquad (35)$$

where $n_1 = 4\kappa_r T_s \Omega_c$, $d_0 = (T_s\Omega)^2 + 4T_s\Omega_c + 4$, $d_1 = 2(T_s\Omega)^2 - 8$, and $d_2 = (T_s\Omega)^2 - 4T_s\Omega_c + 4$. For later use, the discrete-time version of the resonant transfer function, $G_r(s)$ is also required. Tustin discretized resonant transfer function is given by eq. (36):

$$G_r(z) = \frac{(n_1/\kappa_r)\left(1 - z^{-2}\right)}{d_0 + d_1 z^{-1} + d_2 z^{-2}} \qquad (36)$$

For fixed cut-off frequency, i.e., for fixed resonance width of the filter, the expression of eq. (35) has two main tuning parameters. They are the proportional gain κ_p and the resonant gain κ_r. As suggested in [42], these gains can be tuned by comparing the PR controller with the PI controller in the synchronous reference frame, where explicit tuning rules are available for the PI controller. These gains are typically obtained by considering the small-signal model of the overall control system, which is obtained by making several restrictive assumptions. As such, these gains may not be the optimal ones. So, to overcome this limitation, a real-time adaptation of the proportional and resonant gain can be considered as a suitable solution.

In the literature, various intelligent techniques are considered for real-time adaptation of controller gains. Some of these methods are genetic algorithm (GA) [43], particle swarm optimization (PSO) [44], firefly algorithm [45] and neural network (NN) [46, 47]. In general, heuristic optimization-based methods such as GA and PSO are more suitable for offline tuning of the parameters. Methods like neural networks are more suitable for real-time adaptation of control gains. However, conventional neural networks are computationally complex due to the number of hidden layers and other parameters. In this context, ADALINE [48, 49] can be considered as a suitable choice. The ADALINE is one of the earlier single-stage NN architectures proposed in the literature. It has widely been used for many power and energy applications [47, 50].

To develop ADALINE-based online tuning of proportional and resonant gains, let us consider the inputs to ADALINE as e_1 and e_2 where $e_1 = r - y$ is the tracking error with r being the reference and y being the actual output and e_2 is the tracking error passing through the resonant filter (i.e. second term in eq. (36) without the resonant gain). The weights associated with e_1 and e_2 are defined as W_1 and W_2 with the weight vector being $W = \begin{bmatrix} W_1 & W_2 \end{bmatrix}^T$. These weights are the proportional and resonant gains. Then, the synthesis of the PR controller real-time gain adaptation is performed as follows:

$$x(k) = \frac{W_1(k)e_1(k) + W_2(k)e_2(k)}{|W_1(k)| + |W_2(k)|} \qquad (37)$$

$$u(k) = U_{\max} \frac{1 - e^{-x(k)}}{1 + e^{-x(k)}} \qquad (38)$$

where k is the time index and eq. (38) restricts the maximum control magnitude through $U_{\max}$, which is the maximum allowable control amplitude. By using the least-mean square method, the control weights, W_1 and W_2 can be updated using the following update law:

$$W_i(k+1) = W_1(k) + \mu_i e(k) u(k) e_i(k) \qquad (39)$$

where $i = \{1, 2\}$ and μ_i are the learning rate. Thanks to the real-time adaptation of the weights through eq. (39), the control parameters are updated in a self-learning manner where the large error will speed up the learning process. This is particularly important when disturbances occur such as a sudden change in grid voltage and/or load.

3.4. Design of parameters of the VR converter

The line inductance L_f and DC-link capacitor $C_{1,2}$ can be chosen as large as possible to eliminate the current and the voltage ripples. However, the size and cost of the system rise with the stringency of the specification. Assuming having equal $C_1 = C_2$ values of the DC-link capacitors are chosen based on the desired ripple magnitude of the DC-link voltage, which is given as follows [51, 52]:

$$C_1 = C_2 = C > \frac{P_{\text{rate}}}{2\pi\Delta\tilde{v}_{o,dc}f} \qquad (40)$$

where P_{rate} represents the rated power of the VR, $\Delta\tilde{v}_{o,dc}$ is the percentage ripple of the DC-link voltage and f is the grid frequency. Line or filter inductance can be selected to provide continuous line current to reduce the ripple and lower the stress at the switching frequency, f_{sw} [51, 52]. The value of filter inductance can be chosen as follows:

$$L_f > \frac{u_g}{2\Delta I_i P_{\text{rate}} f_{\text{sw}} \eta}\left(1 - \frac{\sqrt{2}u_g}{v_{o,dc}}\right) \qquad (41)$$

where ΔI_i denotes percentage ripple of the line current at the AC side, u_g and η symbolize grid voltage and efficiency, respectively.

3.5. The proposed control structure

The structure of the proposed control algorithm, which includes the DC-link voltage control loop, AC-current control loop, constant battery current control loop and switching signal generation process, is shown in Fig. 2. In addition to the DC-link voltage control, the SMC based outer voltage loop is employed to generate the reference active power, which is used by the current controller (see Fig. 2a). For unity PF, reactive power Q^* is selected as zero. As depicted in Fig. 2b, the ADALINE PR with online tuned proportional and resonant gains is proposed to reduce current errors and track reference current signals compared to the conventional PR control.
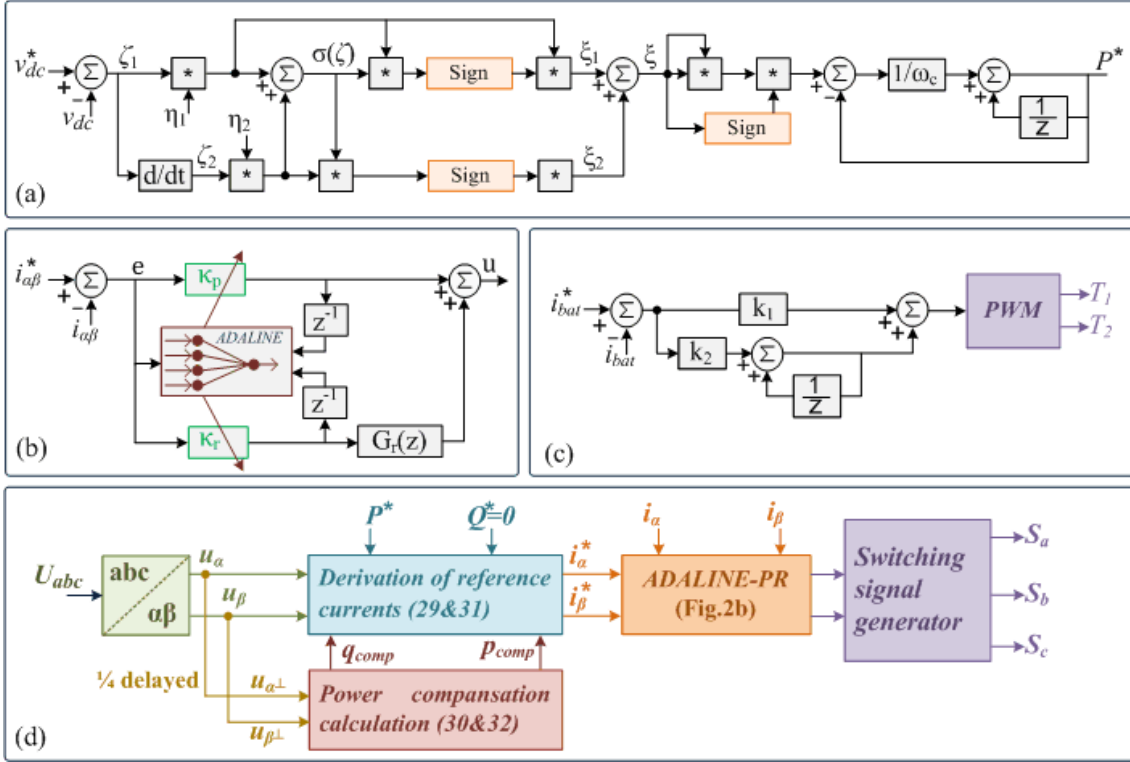
8

Figure 2: The proposed control structure; a) the SMC for the DC-link voltage and active power generation, b) The ADALINE PR control for the source currents, c) constant battery current control of the bidirectional DC-DC converter and d) switching signal generation process for the VR.

A bidirectional DC/DC converter with its control is employed to provide the stable constant battery current without twice grid frequency or second-order harmonic ripples in the power and DC voltage and current, and harmonics during various disturbances at the AC and DC sides (see Fig. 2c). The PI control is used for the constant battery current [53]. Duty cycle of bidirectional switches of the DC-DC converter, d_{conv} can be expressed by eq. (42):

$$d_{\text{conv}} = (I_{\text{bat}}^{\star} - I_{\text{bat}}) \left(k_1 + k_2 \frac{1}{1 - z^{-1}} \right) \qquad (42)$$

where $I_{\text{bat}}^{\star}$ is chosen as the reference battery current and I_{bat} denotes the actual battery current, k_1 and k_2 are the proportional and integral gains of the PI control, respectively.

4. Results And Discussions

In this section, PIL-based quasi real-time study is considered and the considered setup is shown in Fig. 3a. A comparative study between the conventional control as developed in [22] and the proposed control algorithms has been presented under critical cases consisting of dynamic load change, DC-link voltage change, harmonic distorted local loads, grid faults and harmonically distorted grid voltage. Table 1 lists the parameter values of the power circuit and the control algorithm.

Table 1: The key parameters for the proposed test system.

System	Parameters	Value
Utility grid	Line-to-line source voltage (rms)	380V
	Frequency	50Hz
Vienna Rectifier	Switching Frequency	10kHz
	Sampling Frequency	25kHz
	Rated DC-link voltage	600V
	DC-link capacitors, C_1 and C_2	470μF
	Filter inductor (L_f)	2.5mH,
	Filter resistor (R_f)	0.5mΩ
	Fault impedance Z_f	0.01Ω
	DC-link load	$15 - 30\Omega$
SMC	η_1 and η_2	$10, 0.01$
	ω_c	20Hz
Battery Control	k_1 and k_2	$5, 0.01$

4.1. DSP based PIL quasi-real-time results

The performance of the conventional and proposed control algorithm is examined using digital signal processor (DSP) TMS320F28335 within a processor in the loop (PIL) setting in PSIM software environment under different operating conditions as depicted in Fig. 3b. TMS320F28335 DSP control card is employed for running the control algo-
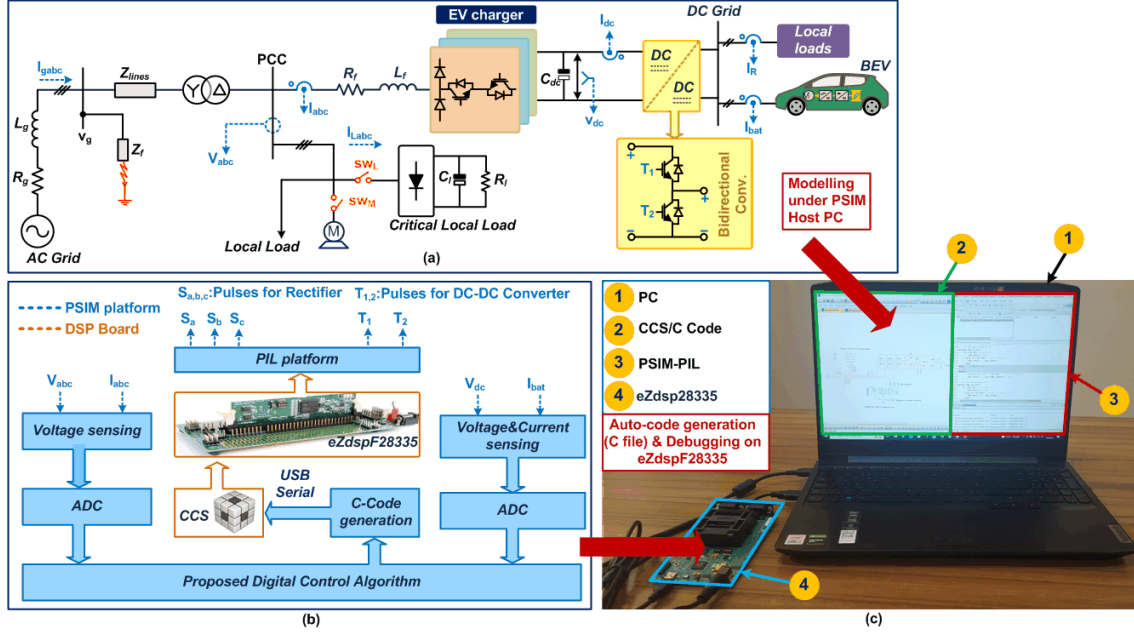
9

Figure 3: Setup for performance verification under various case studies, a) schematic diagram of the test system, b) the switching signals generation process based on the digital control algorithm and c) DSP based PIL test platform.

rithm part while the power circuit comprising the VR, DC-DC converter, battery, local loads and the utility grid runs in PSIM software environment. The generated C-code by the proposed digital control algorithm is connected to code composed studio (CCS) and executed by CCS. The major procedure of the implementation is such that the power system part is directly connected to the PSIM platform while the control algorithm part is loaded and operated into the DSP board through USB/JTAG, at the same time. The photo of the DSP based PSIM-PIL test platform including host PC and Texas Instruments C2000 F28335 is displayed in Fig. 3c. In the following, various case studies are considered. Detailed analysis are presented to examine the performance of the proposed control algorithm.

The steady-state responses of both control algorithms under stepped change in the DC-link voltage and DC load are shown in Fig. 4. The reference DC-link voltage has been suddenly increased at $t = 0.15$ sec. and decreased at $t = 0.2$ sec. The proposed control algorithm ensures better performance in contrast to the conventional control reported in [22]. As observed in Fig. 4a and 4b, while conventional control tracks the reference DC-link voltage within 30 msec. and 35 msec., the proposed control algorithm achieves effective tracking of the DC-link voltage reference within 20 msec. and 25 msec., respectively. Also, as displayed at the bottom of Fig. 4b, similar performance can also be observed for the DC-line current and DC-link power.

As depicted in Fig. 4c and 4d, the dynamic responses of both control algorithms are tested under a step change in the DC load. Here, the DC load has been increased at $t = 0.15$ sec. and decreased at $t = 20$ sec. The waveforms of the DC-link voltage, current and power for the conven-

tional and the proposed algorithm are depicted in Fig. 4c and 4d. The proposed control provides a fast response for the DC-link voltage, DC-line current and DC-link power with 20 msec. and 30 msec. under increased and decreased DC load while the conventional control has a less stable and slower response. The proposed control achieves strong robustness against step change in the load. Also, the phase currents have reached the steady-state earlier with a smooth transient response.

In this scenario, phase b and c voltages experienced 35% voltage drop due to the line to line ground (LLG) grid faults. As observed in Fig. 5a, with the conventional control, three-phase currents of the utility grid have been severely distorted, having a THD of nearly 15%. The DC-link voltage, battery current and DC-link power have double-frequency ripples. On the other hand, as clearly observed in Fig. 5b, the proposed control achieves nearly sinusoidal three-phase currents signals with a lower THD value (2.0%) as well as ensures pure DC battery discharging/charging without the double-frequency harmonic ripples under grid fault conditions. At the LLG grid fault conditions, the conventional control have an outstandingly steady-state error and ripples, i.e, $\Delta \tilde{v}_{o,dc} = 75V(12.5, \Delta I_{o,dc} = 6A$ (15%), while the proposed control provides higher performance with better voltage and current regulation, i.e, $\Delta \tilde{v}_{o,dc} = 6V(0.83, \Delta I_{o,dc} = 0.7A$ (1.75%).

This scenario examines a critical condition under harmonically distorted grid voltages as displayed in Fig. 6 where 5th, 7th, and 11th harmonic components are injected into the balanced grid voltages at $t = 0.15$ sec. It is clearly shown in Fig. 6a that the grid phase currents have significant harmonic contents with a THD of 17% in the case of conventional control method. In contrast, in the case
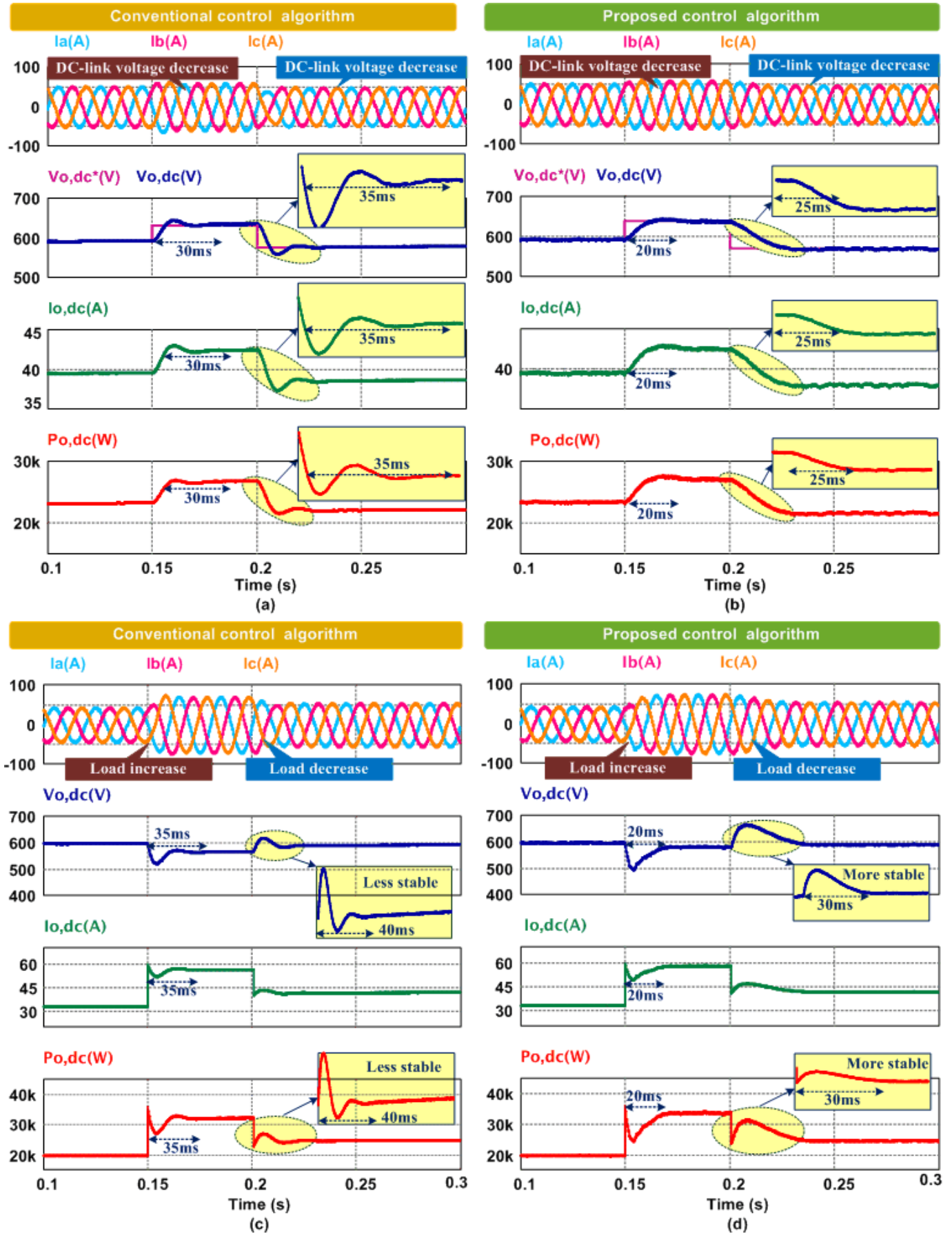
10

Figure 4: Performance evaluation of; a) conventional and b) proposed control algorithms under a stepped change in the DC-link voltage; c) conventional and d) proposed control algorithms under a stepped change in the DC load.
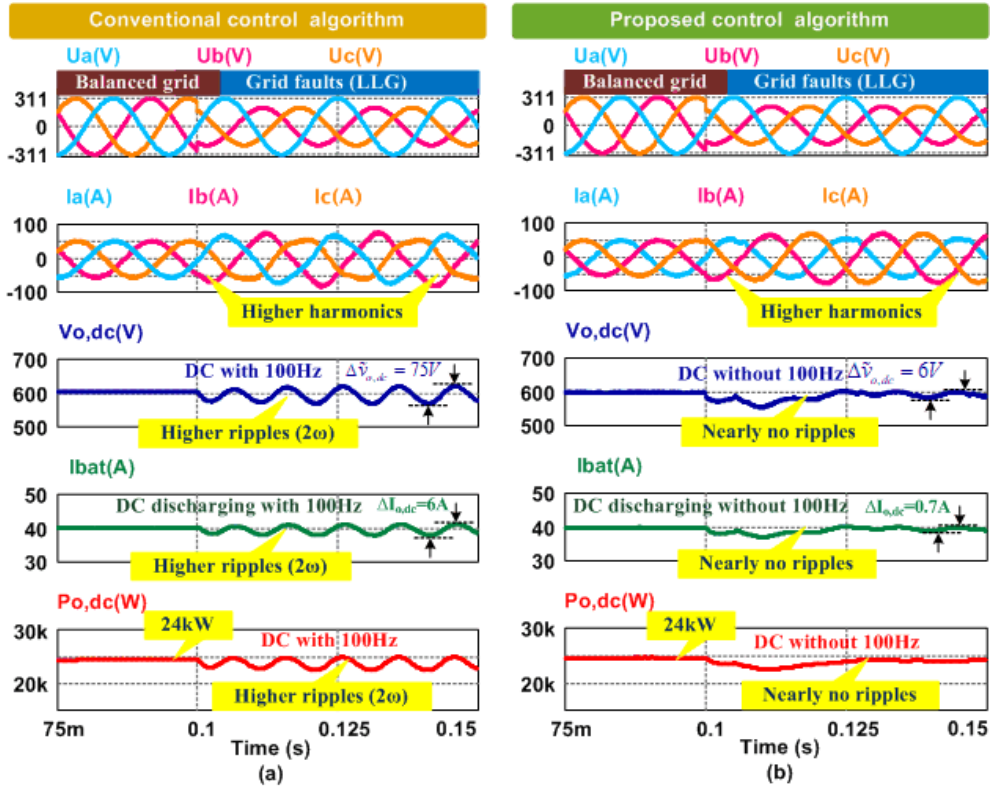
Figure 5: Performance comparison of a) conventional and b) proposed control algorithm under LLG grid fault condition.
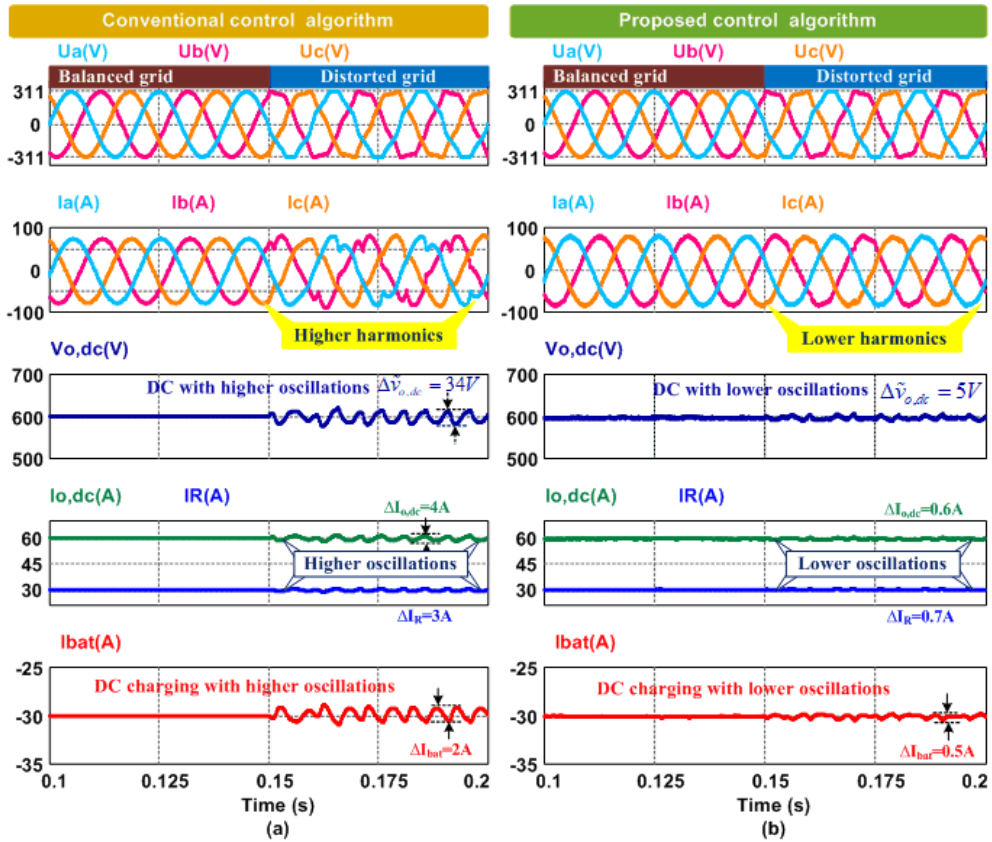

Figure 6: Performance comparison of a) conventional and b) proposed control algorithm under harmonically distorted grid conditions.

of proposed control, the THD of phase currents are nearly 2%, which is considerably lower than that of the conventional control (see Fig. 6b). Compared to the conventional control, the double-frequency harmonic ripples and fluctuations have been protected by the proposed control at the DC-link voltage, battery charging current, DC-line current and load current signals. Besides, with the proposed control, the battery current has been protected against the unbalanced and distorted grid voltage and oscillations and transient fluctuations. Under distorted grid condition, the conventional control exhibits unacceptable performance on the voltage and current regulation as depicted in Fig. 6a. i.e, $\Delta \tilde{v}_{o,dc} = 34V(5.67, \Delta I_{o,dc} = 4A$ (6.67%), $\Delta I_R = 3A$ (10%) and $\Delta I_R = 2A$ (6.67%). The better performance of the proposed control with lower voltage and current ripples is exhibited in Fig. 6b. i.e. $\Delta \tilde{v}_{o,dc} = 5V(5.67, \Delta I_{o,dc} = 0.6A$ (1.0%), $\Delta I_R = 0.7A$ (2.3%) and $\Delta I_R = 0.5A$ (1.67%).

Results in Fig. 7 presents a special scenario where harmonic currents from the local nonlinear load is impacting the power quality. Moreover, a step change in DC load and line to ground (LG) grid fault condition are also considered. Three types of support are being provided by the proposed control algorithm of the EV charging station: i) protection of the DC-link voltage, battery charging current, DC-line current and load current from double-frequency ripples, ii) compensating harmonic currents for the local nonlinear loads and iii) eliminating harmonics of three-phase grid currents caused by the LG grid faults. As depicted at the bottom of Fig. 7a and 7b, the second-order harmonic ripples of the battery charging current are effectively reduced compared to the conventional control. Besides, the grid phase current harmonics are notably mitigated to provide a THD of about $1 - 2\%$ while the harmonics of the conventional control are very high at around 15%. The proposed control algorithm achieves better performance with enhanced voltage and current regulation, and harmonic distortion reduction.

Results presented in Fig. 8 shows the impact of the grid voltage harmonic under unbalanced DC-links. The same harmonic components applied in the case study of Fig. 6 are injected into the utility grid in this case as well. Unbalanced DC-links commonly happen when a VR is employed as a charger for series-tied battery packs. Since the DC-link voltage reference is 600V, the voltage references are 400V and 200V for C_1 and C_2, respectively to create unbalanced DC-links. The oscillations in the DC-link voltage, DC-link current and battery current using the conventional control are slightly larger than that of the proposed control algorithm as shown in Fig. 8b. Numerical values related to the oscillations are presented in Fig. 8a and 8b. Under a balanced and distorted grid, the proposed control algorithm effectively suppresses the harmonics with a THD value of 1% and 2.9% while the line current THD for the conventional control are 5.1% and 7.5%, respectively.

4.2. Discussion and comparison

The THD, efficiency, cost, power density, PF and control circuit complexity are the important aspects of an EV charger. The PF, which is a measure of the efficiency of an electrical system, is significantly affected by distortion of the current waveform. The impact of the THD is measured by the distortion factor (DF) and the impact of the phase displacement of the current first harmonic and the grid voltage are measured by the displacement factor (DPF) or $\cos(\varphi)$ [51, 54–56]. The PF is given by:

$$\text{PF} = \text{DF} \times \text{DPF} = \frac{1}{\sqrt{1 + (\text{THD}_i/100)^2}} \cos(\varphi) \quad (43)$$

where the DF is $1/\sqrt{1 + (\text{THD}_i/100)^2}$ and the DPF is P/S or $\cos(\varphi)$ where S active and apparent power are denoted bu P and S. There is a requirement to reduce harmonic distortions in the EV charging stations. According to the eq. (43) and measured THD values of the conventional and proposed control algorithms, the PF of the proposed control is nearer to the desired unity factor compared to the conventional control. The THD values of 17% and 2% for conventional and proposed control algorithms provide a PF of 0.9759 and 0.9998, respectively. To more intuitively indicate the variation of the source current harmonics, harmonic spectrum analysis of both control algorithms have been presented for grid phase currents as depicted in Fig. 9. The individual harmonic components and THD of the control algorithms are given for easy comparison between the conventional and the proposed control algorithms. As shown in the right of Fig. 9, in all of the cases studied, the THD value of the supply current has been reduced to nearly 2%, which completely complies with the current quality (harmonic) requirements recommended by IEEE-519/IEC 61000 standards.

In Table 2, the performance of the proposed control algorithm is qualitatively compared with the existing methods available in the literature. The PI controller is commonly employed for the DC-link voltage control, but it is difficult to operate in case of parameter variations, load disturbances and nonlinearity. In the existing literature, the gains of the PI, PR control, and PI resonance-sliding mode (PIRSM) [57] have been obtained by utilizing several restrictive assumptions, but these gains may not be optimal. In the proposed control algorithm, a real-time adaptation of the proportional and resonant gains are considered by using the ADALINE neural network. This addresses the non-optimal gain selection issue faced by the conventional control methods. Thanks to the adaptive gain, the proposed method can quickly recover whenever there is a change in the operating condition such as harmonics, grid voltage sag, step change in the DC load and/or the addition of local nonlinear loads. Compared to the other control algorithms as reported in [13, 25, 26, 28], the proposed control has a simple control structure, doesn't require any separation of positive-negative
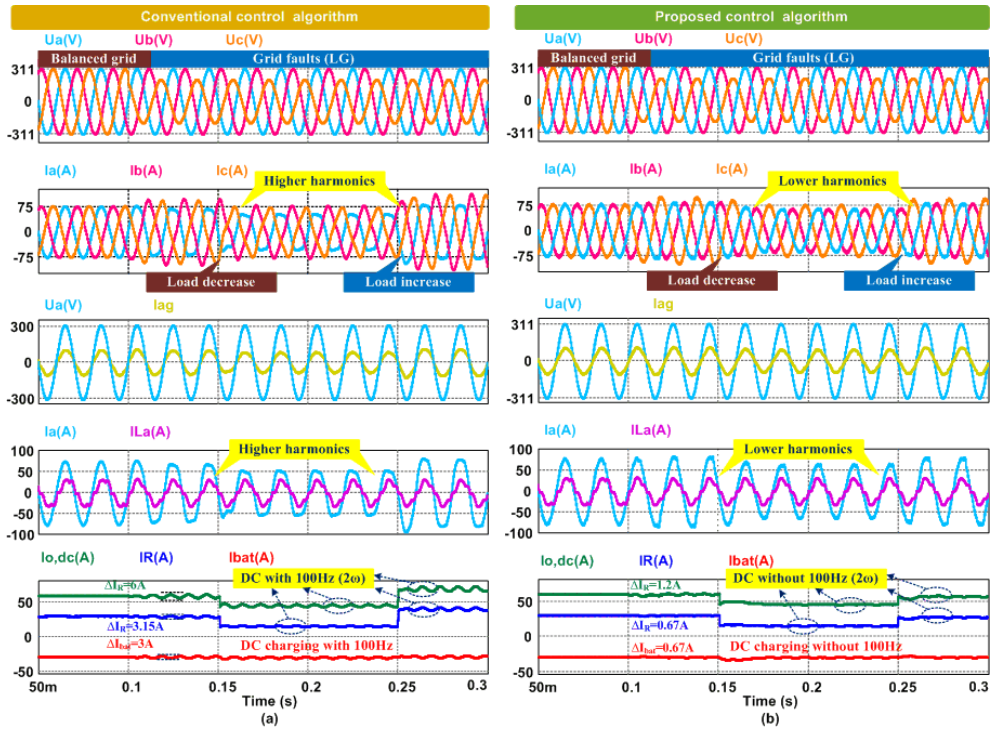
Figure 7: A comparative verification for a) conventional and b) proposed control algorithm under a stepped change in DC load and LG grid fault condition.
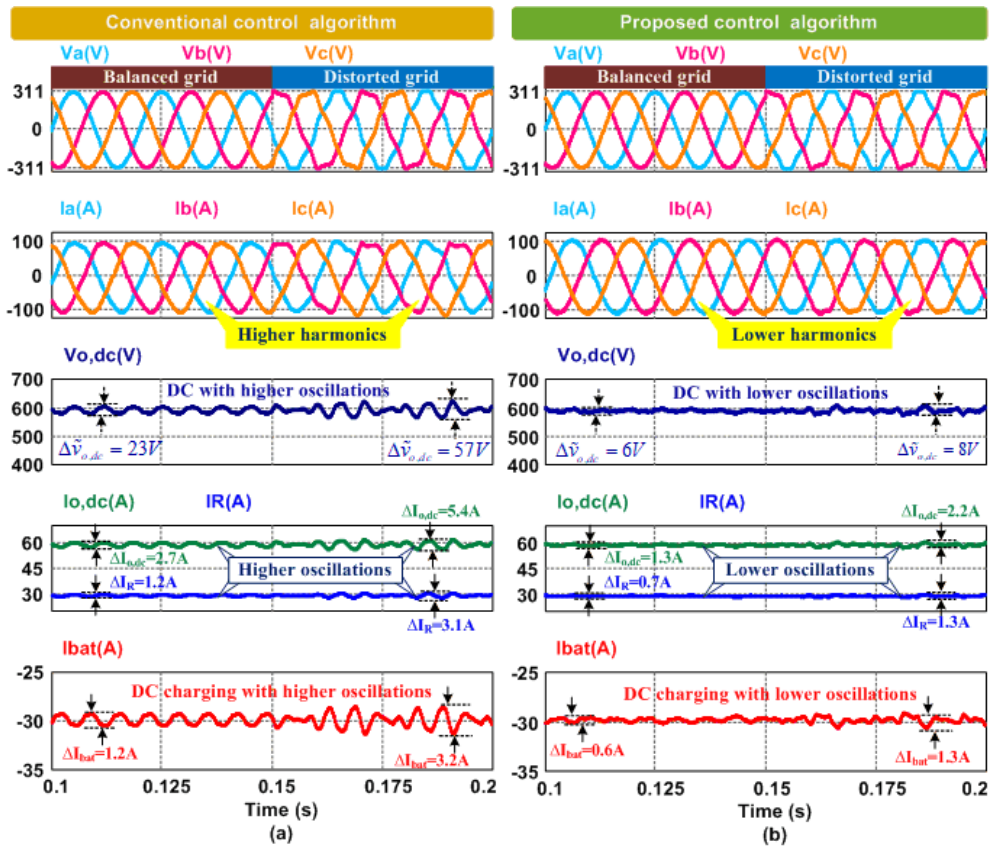

Figure 8: The impact of the grid voltage harmonics under unbalanced DC-link; a) conventional and b) proposed control algorithm.
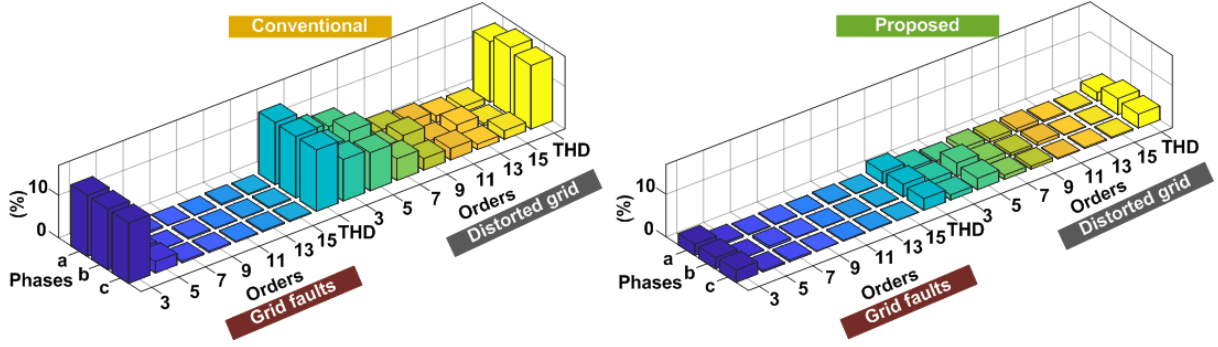
14

Figure 9: The harmonic spectrum analysis of the control algorithms.

sequences and PLL is not needed under unbalance and distorted grid conditions. This makes the proposed control less sensitive to weak grid condition as no PLL is involved. Moreover, by not using any sequence component separation method, the proposed technique avoid the use of additional filters, thereby reducing the computational complexity in terms of number of tunbale gains and real-time implementation. Besides, the harmonics of the source current and ripples in the power and ripples in the DC-link voltage and current are significantly reduced in contrast to studies given in [13, 22, 26, 28, 58]. This has been made possible by the proposed reference current generation method which changes the active and reactive power references according to the grid conditions. In this work, SMC is employed to enhance the dynamic performance of the DC-link voltage instead of the traditional PI control. In [25], linear auto disturbance rejection control (LADRC) has been proposed, but its control structure is complex requiring sequence extraction and PLL. In addition, the harmonics of the source current are high. Although sliding-mode controllers are proposed for current control in [33], however, the DC-link controller remains the conventional PI control. Moreover, the proposed DC-link SMC is very simple to implement unlike the SMC proposed in [33]. A current vector oriented control is presented in [18] to reduce the THD of the line current. Although a control algorithm with a simple structure is proposed in [18, 20], the conventional PI controller is utilized for the DC-link voltage control along with high slow dynamic response and high current harmonics. Predictive controllers are becoming very popular now-a-days for the VR. Predictive controllers reported in [13, 25, 26, 30] mainly need a precise model of the plant and system parameters typically change owing to aging. This controller can also encounter difficulties with significant parameter mismatches. Furthermore, the predictive control utilize a long horizon prediction to increases the stability and to enhance performance of system, but the use of longer-horizon estimations generally increases the computational load of optimization algorithms as a direct trade-off. In addition, parameter mismatch can significantly increase the total harmonic distortion as shown in [24], where 20% reduction in inductor values caused more

than 40% in the total harmonic distortion.

To sum up, the features and performance of the proposed control algorithm are quite superior to those accomplished with state-of-the-art controls in terms of fast dynamic response, lower ripples of the active power, the DC-link voltage and current, reduced complexity of the system, and the THD of the line currents as well as providing a near unity PF.

5. Conclusions and Future Works

In this paper, a new control algorithm based on sliding mode control and the adaptive linear neuron proportional resonant is proposed for the grid interfaced Vienna rectifier to improve the performance of the EV charging stations subject to various disturbances in the source and load side. With the proposed control, the calculation of the power compensation has been designed to eliminate current harmonics and reduce power ripples which leads to significant reduction in the DC-link voltage ripples in the unbalanced and distorted grid condition. The proposed control algorithm effectively mitigates the distorted currents, and ripples of the voltage and current to provide a stable DC-link voltage. Second-order harmonic voltage expressions in the DC-link are also derived to design the DC-link capacitor in an effective way leading to reduce the size and cost of DC-link capacitors. Compared to the existing studies and conventional control, the proportional and resonant gains are online tuned by ADALINE, and the SMC is employed for the DC-link voltage regulation instead of the PI control. The constant and pure battery current during charging/discharging has been provided against various disturbances in contrast to the existing studies in the literature. Besides, a special grid supported mode of the proposed control algorithm is presented to successfully satisfy unbalanced and harmonically distorted currents caused by the local nonlinear load. The comparative results reveal substantial enhancements in terms of fast dynamic response with about 20 msec. settling time and accurate control of the DC-link voltage, sinusoidal and balanced source currents with nearly 2% THD value under various disturbances at the AC and DC

Table 2: Comparison of the proposed control algorithm with other existing studies.

Control algorithm	DC-link control	AC current control	Dynamic response	Source current THD	Power and DC-link ripple	Sequence extraction	PLL	Complexity
[13]	PI	Predictive	Slow	Low	High	Required	Required	Complex
[17]	PI	Voltage vector oriented	Slow	High	Medium	Required	Required	Complex
[18]	PI	Current vector oriented	Slow	Medium	Medium	Required	Required	Complex
[20]	PI	PI	Slow	High	High	Not required	Not required	Simple
[22]	PI	PR	Slow	High	High	Required	Not required	Simple
[24]	PI	Predictive	Slow	High	High	Required	Not required	Complex
[25]	LADRC	Predictive	Fast	High	Low	Required	Required	Complex
[26]	PI	Predictive	Slow	High	High	Required	Required	Complex
[28]	PI	PR	Slow	Medium	High	Required	Required	Complex
[30]	PI	Predictive	Slow	High	Medium	Not required	Not required	Complex
[32]	PI	PR	Slow	High	Low	Not required	Not required	Simple
[57]	PI	PIRSM	Slow	High	Medium	Required	Not required	Complex
[58]	SMC	DPC-SMC	Fast	High	High	Not required	Not required	Simple
Proposed	SMC	ADALINE PR	Fast	Very low	Very low	Not required	Not required	Simple

sides. While the proposed control algorithm achieves approximately 0.8% lower DC-link voltage ripples and 1.0% lower DC-link current and battery current ripples, there are quite large ripples in the DC-link voltage and current with conventional control as reported in [22]. Compared with other control algorithms, the proposed control algorithm provides significant improvements in terms of lower ripples of the active power; lower the DC-link voltage, and battery current ripples, fast dynamic response, less computational burden, and low line current harmonics and near-unity PF. The comprehensive performance comparison of the proposed control algorithm is performed using DSP based PIL quasi real-time setup under several operating conditions.

As a future work, the proposed control algorithm can be implemented to other power electronic systems such as modular multilevel converters, neutral point clamped converters, active power filters, and adjustable speed and motor drives. The proposed control algorithm can also be utilized for any other rectifier topologies. The design and implementation of an active front-end (AFE) rectifier in wind turbine and telecom applications can be considered for power quality improvement. Besides, the high-efficiency AFE rectifier based on the three-level Vienna topology can be employed for various applications such as aircraft electrical systems, industrial battery chargers and equipment, where there are requirements of a low THD and a very high PF.

References

[1] Y. Cao, C. Liu, J. Jiang, X. Zhu, J. Zhou, J. Ni, J. Zhang, J. Pang, M. H. Rummeli, W. Zhou, et al., Theoretical insight into high-efficiency triple-junction tandem solar cells via the band engineering of antimony chalcogenides, Solar RRL 5 (4) (2021) 2000800. doi:10.1002/solr.202000800.

[2] J. Zhou, D. Meng, T. Yang, X. Zhang, Z. Tang, Y. Cao, J. Ni, J. Zhang, Z. Hu, J. Pang, Enhanced charge carrier transport via efficient grain conduction mode for sb2se3 solar cell applications, Applied Surface Science 591 (2022) 153169. doi:10.1016/j.apsusc.2022.153169.

[3] J. Zhou, H. Chen, X. Zhang, K. Chi, Y. Cai, Y. Cao, J. Pang, Substrate dependence on (sb4se6)n ribbon orientations of antimony selenide thin films: Morphology, carrier transport and photovoltaic performance, Journal of Alloys and Compounds 862 (2021) 158703. doi:10.1016/j.jallcom.2021.158703.

[4] Y. Cao, X. Zhu, J. Jiang, C. Liu, J. Zhou, J. Ni, J. Zhang, J. Pang, Rotational design of charge carrier transport layers for optimal antimony trisulfide solar cells and its integration in tandem devices, Solar Energy Materials and Solar Cells 206 (2020) 110279. doi:10.1016/j.solmat.2019.110279.

[5] Y. Cao, X. Zhu, H. Chen, X. Zhang, J. Zhouc, Z. Hu, J. Pang, Towards high efficiency inverted sb2se3 thin film solar cells, Solar Energy Materials and Solar Cells 200 (2019) 109945. doi:10.1016/j.solmat.2019.109945.

[6] D. Xu, Y. Cui, J. Ye, S. W. Cha, A. Li, C. Zheng, A soft actor-critic-based energy management strategy for electric vehicles with hybrid energy storage systems, Journal of Power Sources 524 (2022) 231099. doi:10.1016/j.jpowsour.2022.231099.

[7] W. Wang, Y. Chen, C. Yang, Y. Li, B. Xu, K. Huang, C. Xiang, An efficient optimal sizing strategy for a hybrid electric air-ground vehicle using adaptive spiral optimization algorithm, Journal of Power Sources 517 (2022) 230704. doi:10.1016/j.jpowsour.2021.230704.

[8] X. Zhou, F. Sun, C. Zhang, C. Sun, Stochastically predictive co-optimization of the speed planning and powertrain controls for electric vehicles driving in random traffic environment safely and efficiently, Journal of Power Sources 528 (2022) 231200. doi:10.1016/j.jpowsour.2022.231200.

[9] E. J. Dufek, D. P. Abraham, I. Bloom, B.-R. Chen, P. R. Chinnam, A. M. Colclasure, K. L. Gering, M. Keyser, S. Kim, W. Mai, D. C. Robertson, M.-T. F. Rodrigues, K. Smith, T. R. Tanim, F. L. Usseglio-Viretta, P. J. Weddle, Developing extreme fast charge battery protocols – a review spanning materials to systems, Journal of Power Sources 526 (2022) 231129. doi:10.1016/j.jpowsour.2022.231129.

[10] S. Deb, K. Tammi, K. Kalita, P. Mahanta, Impact of electric vehicle charging station load on distribution network, Energies 11 (1) (2018) 178. doi:10.3390/en11010178.

[11] B. Erdoğan, M. M. Savrun, T. Köroğlu, M. U. Cuma, M. Tümay, An improved and fast balancing algorithm for electric heavy commercial vehicles, Journal of Energy Storage 38 (2021) 102522. doi:10.1016/j.est.2021.102522.

[12] M. Khan, M. Hossain, A. Hossain, A. Ullah, M. S. Hossain Lipu, S. Siddiquee, M. S. Alam, T. Jamal, H. Ahmed, Integration of large-scale electric vehicles into utility grid: An efficient approach for impact analysis and power quality assessment, Sustainability 13 (19) (2021) 10943. doi:10.3390/su131910943.

[13] H. T. Nguyen, A. S. A. Sumaiti, K. A. Hosani, K. A. Jaafari, Y.-J. Byon, J. Y. Alsawalhi, M. S. E. Moursi, Enhanced performance of charging stations via converter control under unbalanced and harmonic distorted grids, IEEE Transactions on Power Delivery 36 (6) (2021) 3964–3976. doi:10.1109/TPWRD.2021.3052319.

[14] S. Ahmad, H. Ahmed, Robust intrusion detection for resilience enhancement of industrial control systems: An extended state observer approach, in: 2022 IEEE Texas Power and Energy Conference (TPEC), 2022, pp. 1–6. doi:10.1109/TPEC54980.2022.9750751.

[15] X. Li, Y. Sun, H. Wang, M. Su, S. Huang, A hybrid control scheme for three-phase Vienna rectifiers, IEEE Transactions on Power Electronics 33 (1) (2018) 629–640. doi:10.1109/TPEL.2017.2661382.

[16] Z. Xu, X. Ren, Z. Zheng, Z. Zhang, Q. Chen, Z. Hao, A quadrature signal based control strategy for Vienna rectifier under unbalanced aircraft grids, IEEE Journal of Emerging and Selected Topics in Power Electronics (2022) 1–1doi:10.1109/JESTPE.2022.3162948.

[17] G. Rajendran, C. A. Vaithilingam, N. Misron, K. Naidu, M. R. Ahmed, Voltage oriented controller based Vienna rectifier for electric vehicle charging stations, IEEE Access 9 (2021) 50798–50809. doi:10.1109/ACCESS.2021.3068653.

[18] D. Mukherjee, D. Kastha, Voltage sensorless control of VIENNA rectifier in the input current oriented reference frame, IEEE Transactions on Power Electronics 34 (8) (2019) 8079–8091. doi:10.1109/TPEL.2018.2878680.

[19] C. Dang, X. Tong, W. Song, J. Huang, Stability analysis of high power factor Vienna rectifier based on reduced order model in d-q domain, Journal of Modern Power Systems and Clean Energy 7 (1) (2019) 200–210. doi:10.1007/s40565-018-0463-8.

[20] S. P. P, R. Kalpana, B. Singh, G. Bhuvaneswari, Design and implementation of sensorless voltage control of front-end rectifier for power quality improvement in telecom system, IEEE Transactions on Industry Applications 54 (3) (2018) 2438–2448. doi:10.1109/TIA.2018.2790949.

[21] Y. Zou, L. Zhang, Y. Xing, Z. Zhang, H. Zhao, H. Ge, Generalized Clarke transformation and enhanced dual-loop control scheme for three-phase PWM converters under the unbalanced utility grid, IEEE Transactions on Power Electronics 37 (8) (2022) 8935–8947. doi:10.1109/TPEL.2022.3153476.

[22] J. Adhikari, P. IV, S. K. Panda, Reduction of input current harmonic distortions and balancing of output voltages of the Vienna rectifier under supply voltage disturbances, IEEE Transactions on Power Electronics 32 (7) (2017) 5802–5812. doi:10.1109/TPEL.2016.2611059.

[23] B. Xu, K. Liu, X. Ran, Q. Huai, Model predictive duty cycle control for three-phase Vienna rectifiers, IET Power Electronics (2022). doi:10.1049/pel2.12244.

[24] B. Xu, K. Liu, X. Ran, Q. Huai, S. Yang, Model predictive duty cycle control for three-phase Vienna rectifiers with reduced neutral-point voltage ripple under unbalanced DC links, IEEE Journal of Emerging and Selected Topics in Power Electronics (2022) 1–1doi:10.1109/JESTPE.2022.3175583.

[25] X. Feng, Y. Sun, X. Cui, W. Ma, Y. Wang, A compound control strategy of three-phase Vienna rectifier under unbalanced grid voltage, IET Power Electronics 14 (16) (2021) 2574–2584. doi:10.1049/pel2.12202.

[26] B. Xu, K. Liu, X. Ran, Computationally efficient optimal switching sequence model predictive control for three-phase Vienna rectifier under balanced and unbalanced DC links, IEEE Transactions on Power Electronics 36 (11) (2021) 12268–12280. doi:10.1109/TPEL.2021.3081771.

[27] Y. Lu, Z. Liu, S. Meng, J. Ji, J. Lyu, Deadbeat predictive power control for Vienna rectifier under unbalanced power grid condition, Energy Reports 7 (2021) 257–266. doi:10.1016/j.egyr.2021.08.048.

[28] L. Hang, H. Zhang, S. Liu, X. Xie, C. Zhao, S. Liu, A novel control strategy based on natural frame for Vienna-type rectifier under light unbalanced-grid conditions, IEEE Transactions on Industrial Electronics 62 (3) (2015) 1353–1362. doi:10.1109/TIE.2014.2364792.

[29] Y. Zhang, J. Liu, H. Yang, J. Gao, Direct power control of pulsewidth modulated rectifiers without DC voltage oscillations under unbalanced grid conditions, IEEE Transactions on Industrial Electronics 65 (10) (2018) 7900–7910. doi:10.1109/TIE.2018.2807421.

[30] H. Zhang, C. Zhang, X. Xing, C. Liu, X. Li, B. Zhang, Three-layer double-vector model predictive control strategy for current

harmonic reduction and neutral-point voltage balance in Vienna rectifier, IEEE Transactions on Transportation Electrification 8 (1) (2022) 251–262. doi:10.1109/TTE.2021.3094320.

[31] P. Zhang, X. Wu, S. He, W. Xu, J. Liu, J. Qi, A. Yang, A second-order voltage ripple suppression strategy of five-level flying capacitor rectifiers under unbalanced AC voltages, IEEE Transactions on Industrial Electronics (2022) 1–1doi:10.1109/TIE.2022.3159958.

[32] Y. Wang, Y. Li, S. Huang, An improved sliding mode direct power control strategy based on reactive power compensation for Vienna rectifier, IEEE Access 10 (2022) 15469–15477. doi:10.1109/ACCESS.2022.3149042.

[33] Y. Fu, N. Cui, J. Song, Z. Chen, C. Fu, C. Zhang, A hybrid control strategy based on lagging reactive power compensation for Vienna-type rectifier, IEEE Transactions on Transportation Electrification 7 (2) (2021) 825–837. doi:10.1109/TTE.2020.3030277.

[34] J.-H. Park, J.-S. Lee, K.-B. Lee, Sinusoidal harmonic voltage injection PWM method for Vienna rectifier with an LCL filter, IEEE Transactions on Power Electronics 36 (3) (2021) 2875–2888. doi:10.1109/TPEL.2020.3011435.

[35] J. Koponen, A. Poluektov, V. Ruuskanen, A. Kosonen, M. Niemelä, J. Ahola, Comparison of thyristor and insulated-gate bipolar transistor-based power supply topologies in industrial water electrolysis applications, Journal of Power Sources 491 (2021) 229443. doi:10.1016/j.jpowsour.2020.229443.

[36] Y. Bi, C. Wu, T. Zhao, H. Li, J. Xu, G. Shu, Y. Wang, Modified deadbeat predictive current control method for single-phase AC-DC PFC converter in EV charging system, IEEE Transactions on Industrial Electronics (2022) 1–1doi:10.1109/TIE.2022.3156151.

[37] Y. Wu, Y. Huangfu, R. Ma, A. Ravey, D. Chrenko, A strong robust DC-DC converter of all-digital high-order sliding mode control for fuel cell power applications, Journal of Power Sources 413 (2019) 222–232. doi:10.1016/j.jpowsour.2018.12.049.

[38] A. Safa, E. M. Berkouk, Y. Messlem, A. Gouichiche, A robust control algorithm for a multifunctional grid tied inverter to enhance the power quality of a microgrid under unbalanced conditions, International Journal of Electrical Power & Energy Systems 100 (2018) 253–264. doi:10.1016/j.ijepes.2018.02.042.

[39] N. Jin, S. Hu, C. Gan, Z. Ling, Finite states model predictive control for fault-tolerant operation of a three-phase bidirectional AC/DC converter under unbalanced grid voltages, IEEE Transactions on Industrial Electronics 65 (1) (2018) 819–829. doi:10.1109/TIE.2017.2686342.

[40] J. Kennedy, P. Ciufo, A. Agalgaonkar, Voltage-based storage control for distributed photovoltaic generation with battery systems, Journal of Energy Storage 8 (2016) 274–285. doi:10.1016/j.est.2016.10.007.

[41] B. Singh, P. K. Dubey, Distributed power generation planning for distribution networks using electric vehicles: Systematic attention to challenges and opportunities, Journal of Energy Storage 48 (2022) 104030. doi:10.1016/j.est.2022.104030.

[42] N. Altin, S. Ozdemir, H. Komurcugil, I. Sefa, Sliding-mode control in natural frame with reduced number of sensors for three-phase grid-tied LCL-interfaced inverters, IEEE Transactions on Industrial Electronics 66 (4) (2019) 2903–2913. doi:10.1109/TIE.2018.2847675.

[43] H. M. Hasanien, S. M. Muyeen, Design optimization of controller parameters used in variable speed wind energy conversion system by genetic algorithms, IEEE Transactions on Sustainable Energy 3 (2) (2012) 200–208. doi:10.1109/TSTE.2012.2182784.

[44] A. K. Mishra, S. R. Das, P. K. Ray, R. K. Mallick, A. Mohanty, D. K. Mishra, PSO-GWO optimized fractional order PID based hybrid shunt active power filter for power quality improvements, IEEE Access 8 (2020) 74497–74512. doi:10.1109/ACCESS.2020.2988611.

[45] S.-A. Amamra, H. Ahmed, R. A. El-Sehiemy, Firefly algorithm optimized robust protection scheme for DC microgrid, Electric Power Components and Systems 45 (10) (2017) 1141–1151.

doi:10.1080/15325008.2017.1319435.

[46] H. K. Khleaf, A. K. Nahar, A. S. Jabbar, Intelligent control of DC-DC converter based on PID-neural network, International Journal of Power Electronics and Drive Systems 10 (4) (2019) 2254. doi:10.11591/ijpeds.v10.i4.pp2254-2262.

[47] G. S. Chawda, A. G. Shaik, Enhancement of wind energy penetration levels in rural grid using ADALINE-LMS controlled distribution static compensator, IEEE Transactions on Sustainable Energy 13 (1) (2022) 135–145. doi:10.1109/TSTE.2021.3105423.

[48] B. Widrow, M. E. Hoff, Adaptive switching circuits, Tech. rep., Stanford Univ Ca Stanford Electronics Labs (1960).

[49] Q. Hu, A. So, W. Tse, A. Dong, Use of adaline PID control for a real MVAC system, in: Proceedings. 2005 International Conference on Wireless Communications, Networking and Mobile Computing, 2005., Vol. 2, 2005, pp. 1374–1378. doi:10.1109/WCNM.2005.1544310.

[50] Z. Chedjara, A. Massoum, P. Wira, A. Safa, A. Gouichiche, A fast and robust reference current generation algorithm for three-phase shunt active power filter, International Journal of Power Electronics and Drive Systems 12 (1) (2021) 121. doi:10.11591/ijpeds.v12.i1.pp121-129.

[51] A. Ali, J. Chuanwen, Z. Yan, S. Habib, M. M. Khan, An efficient soft-switched vienna rectifier topology for EV battery chargers, Energy Reports 7 (2021) 5059–5073. doi:10.1016/j.egyr.2021.08.105.

[52] Y.-W. Kim, J.-H. Kim, K.-Y. Choi, B.-S. Suh, R.-Y. Kim, A novel soft-switched auxiliary resonant circuit of a PFC ZVT-PWM boost converter for an integrated multichip power module fabrication, IEEE Transactions on Industry Applications 49 (6) (2013) 2802–2809. doi:10.1109/TIA.2013.2265074.

[53] M. M. Savrun, M. İnci, M. Büyük, Design and analysis of a high energy efficient multi-port DC-DC converter interface for fuel cell/battery electric vehicle-to-home (V2H) system, Journal of Energy Storage 45 (2022) 103755. doi:10.1016/j.est.2021.103755.

[54] A. Kalair, N. Abas, A. Kalair, Z. Saleem, N. Khan, Review of harmonic analysis, modeling and mitigation techniques, Renewable and Sustainable Energy Reviews 78 (2017) 1152–1187. doi:10.1016/j.rser.2017.04.121.

[55] I. Aretxabaleta, I. M. De Alegría, J. Andreu, I. Kortabarria, E. Robles, High-voltage stations for electric vehicle fast-charging: trends, standards, charging modes and comparison of unity power-factor rectifiers, IEEE Access (2021). doi:10.1109/ACCESS.2021.3093696.

[56] V. Ruuskanen, J. Koponen, A. Kosonen, M. Niemelä, J. Ahola, A. Hämäläinen, Power quality and reactive power of water electrolyzers supplied with thyristor converters, Journal of Power Sources 459 (2020) 228075. doi:10.1016/j.jpowsour.2020.228075.

[57] Y. Zhou, A. Zhang, H. Zhang, J. Huang, W. Yang, L. Zhang, Proportional integral resonance based sliding mode control of VIENNA rectifier for charging station of tramcar under unbalanced power supply, International Transactions on Electrical Energy Systems 30 (10) (2020) e12518. doi:10.1002/2050-7038.12518.

[58] H. Ma, Y. Xie, Z. Shi, Improved direct power control for Vienna-type rectifiers based on sliding mode control, IET Power Electronics 9 (3) (2016) 427–434. doi:10.1049/iet-pel.2015.0149.

18